A Study to Evaluate the Bioactivity Behavior and Electrical Properties of Hydroxyapatite/Ag2O-Borosilicate Glass Nanocomposites for Biomedical Applications
— **Source link** ⎘

Asma M. Alturki, Dalia E. Abulyazied, Dalia E. Abulyazied, Mohammed A. Taha ...+2 more authors

Institutions: University of Tabuk, Egyptian Petroleum Research Institute, Menoufia University

Topics: Microstructure, Nanocomposite, Borosilicate glass and Fourier transform infrared spectroscopy

Related papers:

- Effects of the sintering process on the different properties of alumina/hydroxyapatite nanobiocomposites

- In vitro bioactivity, molecular structure and mechanical properties of zirconia-carbonated hydroxyapatite nanobiocomposites sintered at different temperatures

- Effect of sintering temperature on the morphology, crystallinity and mechanical properties of carbonated hydroxyapatite (CHA)

- Bioactivity and structural properties of nanostructured bulk composites containing Nb2O5 and natural hydroxyapatite

- In vitro bioactivity evaluation, mechanical properties and microstructural characterization of Na2O–CaO–B2O3–P2O5 glasses

A Study To Evaluate The Bioactivity Behavior And Electrical Properties of Hydroxyapatite/Ag$_2$O-Borosilicate Glass Nanocomposites For Biomedical Applications

Asma M. Alturki
   University of Tabuk

Dalia E. Abulyazied
   University of Tabuk

Mohammed Taha (✉ mtahanrc@gmail.com)
   National Research Centre

H. M. Abomostafa
   Menoufia University

Rasha A. Youness
   National Research Centre

Research Article

Abstract

The aim of this work is to prepare nanocomposites with excellent bioactivity and appropriate mechanical properties. In this regard, the nanocomposites, with different contents of borosilicate glass (BG) and carbonated hydroxyapatite (CHA), were mixed and milled using a high-energy ball mill. Then, these milled powders were subjected to sintering at 750 ºC. In order to examine their phase composition, molecular structure and microstructure, X-ray diffraction (XRD) technique, Fourier transform infrared (FTIR) spectroscopy and scanning electron microscopy (SEM), respectively were used. Moreover, the DC electrical conductivity, and physical and mechanical properties of the prepared nanocomposites were also measured. In addition, the in vitro bioactivity of the sintered samples was evaluated using XRD and SEM. Unexpectedly; the results indicated that the successive increase in BG contents promoted the partial decomposition of CHA molecules at this lower sintering temperature. Also, it was responsible for the enhanced bioactivity behavior along with giving CHA better mechanical properties. However, the electrical conductivity of the examined samples exhibited an opposite trend where it decreased significantly with increasing BG content. According to the results obtained, the prepared samples are suitable for use in various biomedical applications.

Introduction

There is a great demand for the continuous development of new prostheses as a result of the tremendous improvements in medicine which have increased the life span of people all over the world [1]. In this regard, this goal can be achieved through many biomaterials such as various metals and their alloys, bioactive glasses, glass-ceramics, calcium phosphates and calcium silicates. In the past few decades, biomaterials have been considered as a hotspot for research as they require many factors that cannot be easily met. One of these important factors is their electrical properties as they are very useful in relieving pain and improving the quality of life. On the other hand, some other are related to their promising biological traits such as bioactivity and biocompatibility [2]. In addition, the ability of the biomaterial to promote cell proliferation along with facilitating bone induction is highly required. It should be noted that these remarkable properties are strongly related to the surface properties of the implant [3]. On the basis of these facts, the researchers believe that bioactive materials such as bioglasses/calcium phosphate compounds are potential candidates for achieving this goal [4].

Hydroxyapatite (HA; $Ca_{10}(PO_4)_6(OH)_2$) is a member of the calcium phosphate family and is found naturally in human and animal bones. Therefore, it has many amazing properties like high surface area, fair bioactivity, excellent biocompatibility, etc. Moreover, its biological and surface properties can be improved by incorporating carbonate $(CO_3)^{2-}$ ions into its crystal structure forming carbonated hydroxyapatite (CHA) and preparing it at the nano-scale range, respectively [5, 6]. Although these remarkable properties, HA has several drawbacks such as low mechanical properties and relatively slow bone bonding ability. Therefore, in order to solve these unwanted defects, adding some elements or ceramics can be a useful solution to face these problems [7−9].

Bioglasses (BGs) have attracted great attention in the past few decades due to their ability to gradually dissolve when implanted into the human body leading to a controlled release of some beneficial ions that promote bone bonding capacity [1]. BGs were first detected by Hench *et al.* [10] in the 1970s and since then, intense efforts have continued to discover new types of BGs to be ideal candidates for the purpose of bone replacement. It is worth to mention that the major benefit of these glasses is their ability to induce the body's own repair process called "osteostimulation" [11, 12]. One of the main groups of these glasses is the borosilicate group which deserves the attention of many researchers as a successful scaffold material. The reason for such interest is its faster absorption rate compared to silicate glass [13].

Extensive research has been conducted to study HA/polymers [14–16] or HA/ceramics composites [17–20]. However, at least to the knowledge of the authors, the study of HA/borosilicate bioglass nanocomposites still needs great attention; especially with measuring their electrical properties. In our attempt to contribute to highlighting these important nanocomposites, the effect of adding low contents of borosilicate, up to 20%, to HA was studied, and it was found that this addition was effective in improving its mechanical and bioactivity [21]. In continuation of these efforts, the present work is concerned with adding glass, with relatively higher contents up to 32%, to HA and raising the sintering temperature to 750 C and studying the effect of these factors on the in vitro bioactivity, mechanical and electrical properties of these nanocomposites.

Experimental Procedure

2.1. Preparation of bioactive glass (BG) samples

Glass system has been prepared by melting the starting materials (SiO_2, H_2BO_3, Na_2CO_3, $CaCO_3$ and $AgNO_3$) in a platinum crucible at 1100°C for 2 h in air. In order to ensure a homogenous mixing of all reactants and get a bubble-free sample, the molten liquid was stirred to ensure homogenous mixing of all constituents. Then, the batches were poured in a mold with the desired shape and instantly put in another muffle to be annealed at about 380–400°C for 1 h. Subsequently, the muffle was switched off and the temperature decreased to room temperature with a rate of 25°C/h. The nominal composition of the prepared glass system is tabulated in Table 1.

Table 1
Nominal composition (wt.%) of Ag_2O-containing borosilicate glass.

Oxide	Content (wt.%)
SiO_2	5
B_2O_3	40
Na_2O	20
CaO	25
Ag_2O	10

2.2. Preparation of CHA nanopowders

The CHA nanopowders were prepared with the help of Refs. [22, 23] and they were characterized by the use of XRD technique and FTIR spectroscopy. Briefly, a high-energy ball mill was used using calcium carbonate ($CaCO_3$) and calcium hydrogen phosphate dihydrate ($CaHPO_4 \cdot 2H_2O$) as raw materials for the preparation of CHA nanopowders having in mind that the success of the mechanochemical synthesis method for producing CHA depends on many parameters like the ball-to-powder ratio (BPR) and milling time because they enhance the occurrence of the reaction. To better elucidate the morphology of the as-synthesized CHA nanopowders, scanning electron microscopy-coupled with energy dispersive spectroscopy (SEM-EDS, type Quanta FEG250) with an acceleration voltage of 30 kV and a magnification 10× up to 300,000× was used.

2.3. Preparation of CHA/BG nanocomposites powders

The CHA and BG, based on their weight%, represented in Table 2, were blended by a high-energy ball mill for 10 h with BPR equal to 1:2 and the diameter of balls was 10 mm. Subsequently, these mixtures were milled for 5 h in a high-energy ball mill operating at 400 rpm as a rotation speed and BPR = 20:1. Noteworthy, the milling has been performed under dry condition.

Table 2

Scheme of the prepared nanocomposites indicating the sample code and its composition as weight percentage (wt.%).

Sample code	Bioactive glass (BG)	Carbonated hydroxyapatite (CHA)
HG0	0	100
HG1	4	96
HG2	8	92
HG3	16	84
HG4	32	68

2.4. Measurement of the different properties of CHA/BG nanocomposites

2.4.1. Physical properties

Based on the recent articles of Taha *et al.* [24, 25], the milled powders were pressed into pellets of 16 mm in diameter and 4 mm in length using hydraulic press at 50 MPa. Archimedes' method (ASTM: B962-13) was employed for determining bulk density and apparent porosity of the sintered samples at 750°C.

2.4.2. Mechanical properties

According to the references [26–28], the microhardness and compressive strength of the examined samples were measured. Additionally, Poisson's ratio and the values of elastic moduli; Young, elastic, bulk and shear modulus were calculated according to the reference [29].

2.4.3. Electrical properties

The DC electrical conductivity of the prepared nanocomposites was measured at room temperature using a Keithley 616.

2.5. Characterization of the sintered samples

The phases formed in the nanocomposite samples result from sintering process were identified using X-ray diffraction (XRD) technique, "Philips PW 1373" X-ray powder diffractometer with CuK-Ni filtered radiation. In order to confirm the chemical composition of the prepared nanocomposites, Fourier transform infrared (Vertex 80, Bruker, Germany) spectroscopy was used. The FTIR absorption spectra of the tested nanocomposites were immediately collected by the attenuated total reflection (ATR) unit, at room temperature, in the wavenumber range $4000-400$ cm^{-1}, 60 scans with a resolution 4 cm^{-1}. Moreover, SEM was also used to examine the microstructure of these samples.

2.6. The evaluation of the in vitro bioactivity of sintered nanocomposites

The in vitro bioactivity of the resulting nanocomposites was assessed by soaking the sintered nanocomposites for 10 days in a simulated body fluid (SBF) prepared according to the recipe described by Kokubo *et al.* [30, 31] while maintaining the ratio of glass grains to volume of solution = 0.01 g/ml [32]. Then, the soaked samples were subjected to XRD and SEM to examine the HA layer formed on their surfaces.

Results And Discussion

3.1. The different properties of CHA/BG nanocomposites

3.1.1. Physical properties

The densification behavior of the material is closely related to the removal of porosity present in the sintered sample bearing in mind that the presence of nano-sized CHA powders is effective in improving the densification behavior by closing the pores [33, 34]. Moreover, the glass contents in the nanocomposites along with the selected sintering temperature are expected to have an important role in enhancing the condensation manner [35, 36]. On this basis, the bulk density and apparent porosity of the sintered nanocomposites were measured as shown in Fig. 1 (a,b). From this figure, it is possible to see that the successive increases in BG content positively affected the bulk density. On the contrary, this increase in BG content reduces the porosity of the sintered nanocomposites. As previously discussed in references [5, 20], good densification behavior depends on the sintering temperature while carrying out the sintering process through three stages. First, the compaction of powders facilitates contact formation. Second, the particles are closely bonded due to the creation of "necks" between them. Notably, these nicks are formed when the sintering temperature reaches two-thirds of the melting point. Finally, the particles are full bonded, and cannot be seen individually and the remaining porosity is closed-off.

3.1.2. Mechanical properties

Generally, the sintered glass samples show better mechanical properties compared to those of the original glass provided the sintering process is carried out under suitable conditions [37]. Therefore, microhardness, compressive strength, Young's modulus, elastic modulus, bulk modulus, shear modulus and Poisson's ratio of all sintered nanocomposites were measured and represented in Figs. (2−4). All mechanical properties of the examined nanocomposites exhibit marked increases with successive increases in the BG content. As will be explained in the next section, although CHA was partially decomposed giving β-tricalcium phosphate (β-TCP; $Ca_3(PO_4)_2$) which in turn, leads to a marked decrease in the mechanical properties of the sintered samples, this effect was largely offset by the existence of grains in the nano-scale range which considerably improves the mechanical properties. The results obtained are supported by Refs. [38−40]. Most importantly, understanding the relationships between porosity and mechanical properties is essential to take advantage of the porosity to improve the bioactivity behavior of the prepared samples without sacrificing their mechanical properties [22].

3.1.3. Electrical properties of the sintered nanocomposites

Generally, electrical stimulation is known to enhance the rate of bone growth and thus reduce healing time [41–43]. Based on this principle, it is important to study the electrical response of the prepared nanocomposites. In this regard, the DC conductivity of all prepared nanocomposites was measured as shown in Fig. 5. As can be seen from this figure, the successive addition of glass, up to 32 wt.%, to CHA was responsible for a significant decrease in the DC conductivity from 1.34×10^{-8} to 1.7×10^{-9}. The reason of this result is that borosilicate glass has a high electrical resistance, i.e. 10^{11}-10^{13} Ωm [44]. Based on that fact, 10 wt.% of Ag_2O content is insufficient to significantly improve the electrical conductivity.

Although the conduction mechanism of HA is not clear, the proposed conductive species are ions such as protons (H^+), oxide (O^2) and hydroxyl (OH^-) [45]. Some published articles excluded the effect of Ca and PO_4^{3-} ions and stated that the ionic conductivity of HA is mainly due to the presence of OH^- ions within the c-axis columns and thus, it is considered a one-dimensional anionic conductor. This assumption was confirmed by electrolysis measurements which revealed that OH^- ions are considered charge carriers [46–49]. The results obtained are in a good agreement with those reported in Refs. [2, 46].

3.2. Characterization of the sintered samples

3.2.1. XRD analysis

It is known that heat treatment of prepared glass samples is responsible for converting them into corresponding glass-ceramic. Importantly, the amount of the remaining glass composition, and the resulting crystalline phases and their quantities depend on the properties of the glass as well as the conditions of the heat treatment process [50]. Because of these facts, XRD technique is favorable for determining the phases produced as a result of heat treatment. Therefore, XRD patterns were recorded for all sintered nanocomposites specimens as represented in Fig. 6. A precise analysis of the obtained XRD patterns indicates that there are distinct peaks of CHA (JCPDS No. 19–0272) only for the HG0 sample. However, the HG1 sample exhibits an inconsiderable decrease in the intensity of some of characteristic peaks of CHA. This decrease could be attributed to the addition of 4 wt.% of BG, at the expense of CHA, or a very slight degeneration of CHA and formation of β-TCP that falls below the XRD instrument detection limit. For the HG2 sample, the distinct peaks belonging to CHA appear beside those of the β-TCP phase identified according to (JCPDS No. 03-0691). Interestingly, the characteristic hump of the glasses that results from lack of lattice periodicity is not present in all tested samples, indicating that the specified sintering temperature effectively crystallized these glasses to their corresponding glass-ceramics. Of note, these results obtained are inconsistent with those stated in Ref. [23] which discussed that CHA nanopowders prepared by the mechanochemical synthesis method possesses high thermal stability even after exposure to 1000 ºC. These results can be explained in terms of the presence of BG which encourages the decomposition of CHA at this lower temperature giving the characteristics peaks of the above phases due to the expulsion of some OH^- groups. For the HG3 sample, the CHA peaks show significant decreases in their intensity coupled with considerable increases in the intensity of the peaks characteristic of β-TCP phase due to an increased influence of BG on the incidence of partial

decomposition of CHA. Also, three new phases; namely calcium borate (CaB_2O_4; JCPDS No. 76−0747), sodium borate ($NaBO_2$; JCPDS No. 12−0492) and calcium sodium borate ($CaNaB_5O_9$; JCPDS No. 37−0827) are clearly shown. Finally, the new phase representing the crystalline silver oxide phase (Ag_2O; JCPDS No. 76-1393) appears in the HG4 sample along with the above mentioned phases.

Most of the published crystallization research [51−53] has focused on silicate bioactive glasses and very few ones have been devoted to borate and phosphate glasses. In this regard, this study is an effort to contribute to the interest in studying the effect of sintering temperature on crystallization of borosilicate bioactive glasses. As described in Ref. [54], the presence of metal oxides such as Ag_2O along with the heat treatment process is a major reason for the phase separation and the subsequent crystallization process.

3.2.2. Structural analysis using FTIR spectroscopy

Generally, FTIR spectroscopy is a valuable technique for identifying basic structural groups in prepared samples. Therefore, the FTIR absorption spectra of all prepared nanocomposites were collected as shown in Fig. 7 while they were interpreted with the help of literature [5, 55−58]. Careful examination of the FTIR spectra reveals the following:

- The characteristic bands belonging to CHA at 1630, 1460, 1420, 1100, 1035, 980, 870, 630, 605, 560 and 470 cm^{-1} are clearly visible in the HG0 sample. As expected, no other bands in this spectrum have been seen.

- In the HG1 sample, the aforementioned bands showed noticeable decrease in their intensity due to the slight decomposition that has occurred in the CHA molecule forming the β-TCP phase and addition of BG at the expense of CHA.

- In the HG2 sample, the intensity of the characteristic bands of CHA molecules continued to decrease with a further increase in the BG content to 8 wt.%. It is important to note that although the β-TCP phase formation usually results in a considerable band located at 1100 cm^{-1} towards a higher wavenumber, i.e. 1120 cm^{-1}, this shift has not been observed in the spectrum of this sample. The absence of this shift can be attributed to the fact that the majority of CHA molecules were not decomposed, and thus the main band at 1100 cm^{-1} is dominant.

- A new band belonging to the stretching modes of the B-O bonds of the BO_4 groups is clearly seen at 1200 cm^{-1} with a considerable increase in the intensity of band located at 940 cm^{-1} in the HG3 sample considering that the latter band interferes with the vibration mode of the O-P-O bond in CHA molecules. Moreover, the bending vibration modes of different groups of borate can be confirmed by a single weak band at 780 cm^{-1} with increasing weak band intensity at 870 cm^{-1}. As expected, the increase in their intensity correlated closely with the increase in BG content. These findings are in strong agreement with the XRD results discussed in the former section as two different borate phases; namely CaB_2O_4 and $Na_2B_4O_7$ phases are seen as a result of increasing the BG content up to 16 wt.%.

- A considerable broadness in the absorption band at 560 cm^{-1} was recorded in the HG4 specimen. This broadness is attributed to the vibration mode of crystalline Ag_2O phase which interferes with the bending vibrations of the O-P-O bonds in the PO_4^{3-} groups.

It is important to note that no vibrations were detected for the crystalline phases belonging to SiO_2 as its contribution to the formation of the prepared glass is about 5 wt.%. Hence, the addition of this glass at 32 wt.% is insufficient to appear.

3.2.3. Microstructural analysis using SEM

In general, the different biomedical applications of materials are strongly determined by their morphology [18]. Based on this fact, SEM coupled with EDS was employed to examine the morphology of the as-prepared CHA nanopowders as shown in Fig. 8 (a,b). Moreover, SEM was also used to investigate the microstructure of the HG0, HG2 and HG4 sintered samples as illustrated in Fig. 9 (a-c). As can be seen from Fig. 8a, the synthesized CHA is mainly composed of spherical particles with a large amount of agglomeration since the mechanochemically prepared materials usually show high agglomeration [18]. It is important to note that the presence of this agglomeration in the synthesized apatite sample is beneficial, according to the literature, as it allows the circulation of body fluids when this sample is applied as a coating on the implant [59]. The elemental analysis of the prepared CHA, as shown in Fig. 8b, reveals the existence of Ca, P, O and C peaks. On the contrary, the sintered CHA sample, i.e. HG0 appears to have spherical particles with a number of needle-shaped particles with uniform distribution. This recorded change in the morphology may be attributed to the sintering process of CHA at 750 °C which agrees, to some extent, with those reported in Refs. [60, 61]. Figure 9b shows that the needle-shaped particles disappeared as a result of the addition of BG to CHA at 8 wt.% with partial decomposition that occurred in the CHA particles in agreement with the XRD results. It should be noted that the particles can be easily seen individually due to the large number of porosity. This finding is highly supported by the density results discussed in Sect. 3.1.1. By increasing the BG content up to 32 wt.%, Fig. 9c, the porosity is greatly reduced and thus, the particles are no longer seen individually. These observations are well consistent with the results for XRD, density and porosity.

3.3. In vitro bioactivity assessment of sintered nanocomposites

3.3.1. XRD analysis

It is well known that immersion of bioactive substances in SBF solution allows them to react with ionic concentrations equivalent to human blood plasma, forming hydroxyapatite layer on their surfaces. Therefore, all sintered nanocomposites were dipped in SBF solution for 10 days and then subjected again to XRD to confirm the formation of the required apatite layer as shown in Fig. 10. It is possible to see from this figure that all the tested nanocomposites show good bioactivity considering that the increased BG content is responsible for increasing the bioactivity of the nanocomposites. Therefore, the best bioactivity among all samples is that of the HG4 sample where it contains 32 wt.% of bioactive glass

which has better bioactivity compared to that of CHA. Unfortunately, the decomposition that occurs in the CHA molecules and the formation of β-TCP due to the increased BG content reduces the bioactivity of the examined samples due to the rapid dissolution rate of the β-TCP phase in the SBF solution. This interpretation is highly supported by the absence of this phase in the figure which is consistent with Refs. [18, 29].

3.3.2. Microstructural characterization by SEM

In this work, SEM was used to examine the apatite layer formed on the surface of the HG4 sample after it was immersed in SBF solution for 10 days as illustrated in Fig. 11. From this image, one can see that increasing the BG content to 32 wt.% is a major reason for the formation of a relatively dense apatite layer on its surface. The reader can note that the dependence of this study on determining the formation of the apatite layer on XRD rather than SEM technique. The reason for this reliance is its ability to detect this desired layer throughout the entire sample, which gives more accurate results, and therefore, it provides us with the information required to choose the sample with the best bioactivity among all. On the contrary, SEM is useful for giving readers only the visual note.

Conclusions

In this study, a borosilicate glass (BG) sample containing the composition: $5SiO_2$-$40B_2O_3$-$20Na_2O$-$25CaO$-$10Ag_2O$ (wt.%) was prepared by conventional melt-quenching method. On the other hand, carbonated hydroxyapatite (CHA) nanopowders were prepared following the mechanochemical synthesis method described in our recent articles. Then, different contents of this glass sample, i.e. 0, 4, 8, 16 and 32 wt.% have been added to the CHA nanopowders with the help of mechanical alloying method, consolidated and sintered at 750 ºC. The physical, mechanical and electrical properties of the sintered nanocomposites were measured in terms of bulk density, apparent porosity, microhardness, compressive strength, Poisson's ration, and Young's, elastic, bulk, shear moduli, and DC conductivity. Moreover, the prepared samples were characterized using different tools such as Fourier transform infrared (FTIR) spectroscopy, X-ray diffraction (XRD) technique and scanning electron microscopy (SEM). Also, the bioactivity behavior of the nanocomposites after soaking in SBF solution for 10 days was evaluated with the help of XRD and SEM techniques. Analysis of the XRD patterns clarified that the chosen sintering temperature was sufficient to induce complete crystallization in the selected glass system giving calcium borate (CaB_2O_4), sodium tetraborate ($Na_2B_4O_7$), crystalline silver oxide (Ag_2O) and β-tricalcium phosphate ($Ca_3(PO_4)_2$) phases beside CHA ($Ca_{10}(PO_4)_6(OH)_2$). It should be noted that both the bioactivity and mechanical properties were improved with the increase of BG content in the examined samples. In contrast, DC conductivity was negatively affected by this increase in BG content.

Declarations

Acknowledgement

References

1. V.V.A. Thampi, B. Subramanian, Bioactive glasses for orthopedic and orthodontic implant applications, Elyns J. Mater. Sci. Tech. 1 (1) (2017): 1-10.

2. A. Das, D. Pamu, A comprehensive review on electrical properties of hydroxyapatite based ceramic composites, Mater. Sci. Eng. C 110 (2019): 539-563.

3. J.N. Olivera, Y. Suc, X. Lua, P.-H. Kuoa, J. Dua, D. Zhuc, Bioactive glass coatings on metallic implants for biomedical applications, Bioact. Mater. 4 (2019): 261-270.

4. S. Seyedmajidi, R. Rajabnia, M. Seyedmajidi, Evaluation of antibacterial properties of hydroxyapatite/bioactive glass and fluorapatite/bioactive glass nanocomposite foams as a cellular scaffold of bone tissue, J. Lab. Physicians 10 (3) (2018): 265-270.

5. R.A. Youness, M.A. Taha, A.A. El-Kheshen, M. Ibrahim, Influence of the addition of carbonated hydroxyapatite and selenium dioxide on mechanical properties and in vitro bioactivity of borosilicate inert glass, Ceram. Int. 44 (2018): 20677-20685.

6. R.A. Youness, M.A. Taha, M. Ibrahim, In vitro bioactivity, physical and mechanical properties of carbonated-fluoroapatite during mechanochemical synthesis, Ceram. Int. 44 (2018): 21323-21329.

7. E.S. Thian, T. Konishi, Y. Kawanobe, P.N. Lim, C. Choong, B. Ho, M. Aizawa, Zinc substituted hydroxyapatite: a biomaterial with enhanced bioactivity and antibacterial properties, J. Mater Sci. Mater Med. 24 (2013): 437-445.

8. P. Bhattacharjee, H. Begam, A. Chanda, Development and physical, chemical and mechanical characterization of doped hydroxyapatite, Int. J. Sci. Eng. Res. 2 (4) (2011): 1-8.

9. H. Oonishi, Orthopaedic applications of hydroxyapatite, Biomaterials 12 (1991): 171-178.

10. L.L. Hench, R.J. Splinter, W.C. Allen, T.K. Greenlee, Bonding mechanisms at the interface of ceramic prosthetic materials,
    J. Biomed. Mater. Res. 2 (1971): 117-141.

11. L.L. Hench, J.R. Jones, Bioactive glasses: frontiers and challenges. Front Bioeng Biotechnol 3 (2015): 1-12.

12. H. Oonishi, L.L. Hench, J. Wilson, F. Sugihara, E. Tsuji, M. Matsuura, Quantitative comparison of bone growth behavior in granules of Bioglass (R), A-W glass-ceramic, and hydroxyapatite, J Biomed Mater Res. 51 (1) (2000): 37-46.

13. X. Qi, H. Wang, Y. Zhang, L. Pang, W. Xiao, W. Jia, S. Zhao, D. Wang, W. Huang, Q. Wang, Mesoporous bioactive glass-coated 3D printed borosilicate bioactive glass scaffolds for improving repair of bone defects, Int. J. Biol. Sci. 14 (4) (2018): 471-484.

14. I.J. Macha, B. Ben-Nissan, J. Santos, S. Cazalbou, A. Stamboulis, D. Grossin, G. Giordano, Biocompatibility of a new biodegradable polymer-hydroxyapatite composite for biomedical

applications, J. Drug Deliv. Sci. Technol. 38 (2017): 72-77.

15. G. Dubinenko, A. Zinoviev, E. Bolbasov, A. Kozelskaya, E. Shesterikov, V. Novikov, S. Tverdokhlebov, Highly filled poly(1-lactic acid)/hydroxyapatite composite for 3D printing of personalized bone tissue engineering scaffolds, J. Appl. Polym. Sci. 138 (2) (2020): 1-10.

16. S. Sathiyavimal, S. Vasantharaj, F.L. Oscar, R. Selvaraj, K. Brindhadevi, A. Pugazhendhi, Natural organic and inorganic-hydroxyapatite biopolymer composite for biomedical applications, Prog. Org. Coat. 147 (2020) 105858.

17. R.A. Youness, M.A. Taha, M. Ibrahim, In vitro bioactivity, molecular structure and mechanical properties of zirconia-carbonated hydroxyapatite nanobiocomposites sintered at different temperatures, Mater. Chem. Phys. 239 (2020) 122011.

18. M.A. Taha, R.A. Youness, M. Ibrahim, Biocompatibility, physico-chemical and mechanical properties of hydroxyapatite-based silicon dioxide nanocomposites for biomedical applications, Ceram. Int. 46 (2020): 23599-23610.

19. R.A. Youness, M.A. Taha, M. Ibrahim, Effect of sintering temperatures on the in vitro bioactivity, molecular structure and mechanical properties of titanium/carbonated hydroxyapatite, J. Mol. Struct. 1150 (2017): 188-195.

20. R.A. Youness, M.A. Taha, M.A. Ibrahim, The influence of various zirconia contents on crystallite sizes, shrinkage, and physical and mechanical properties of hydroxyapatite-based nanobiocomposites, Egypt. J. Chem. 64 (3) (2021): 1347-1352.

21. D.E. Abulyazied, A.M. Alturki, R.A. Youness, H. M. Abomostafa, Synthesis, structural and biomedical characterization of hydroxyapatite/borosilicate bioactive glass nanocomposites, J. Inorg. Organomet. Polym. Mater. (2021) In Press.

22. R.A. Youness, M.A. Taha, H. Elhaes, M. Ibrahim, Molecular modeling, FTIR spectral characterization and mechanical properties of carbonated hydroxyapatite prepared by mechanochemical synthesis, Mater. Chem. Phys. 190 (2017): 209-218.

23. R.A. Youness, M.A. Taha, H. Elhaes, M. Ibrahim, Preparation, FTIR characterization and mechanical properties of hydroxyapatite nanopowders, J. Comput. Theor. Nanosci. 14 (2017): 2409-2415.

24. E.B. Moustafa, M.A. Taha, Evaluation of the microstructure, thermal and mechanical properties of Cu/SiC nanocomposites fabricated by mechanical alloying, Int. J. Miner. Metall. Mater. 28 (2021): 475-486.

25. E.B. Moustafa, W.S. AbuShanab, E. Ghandourah, M.A. Taha, Microstructural, mechanical and thermal properties evaluation of AA6061/Al_2O_3-BN hybrid and mono nanocomposite surface, JMRT 9 (6) (2020): 15486-15495.

26. W.S. AbuShanab, E.B. Moustafa, E. Ghandourah, M.A. Taha, Effect of graphene nanoparticles on the physical and mechanical properties of the Al2024-graphene nanocomposites fabricated by powder metallurgy, Results Phys. 19 (2020) 103343.

27. R.A. Youness, M.A. Taha, A. El-Kheshen, N. El-Faramawy, M. Ibrahim, In vitro bioactivity evaluation, antimicrobial behavior and mechanical properties of cerium-containing phosphate glasses, Mater.

Res. Express 6 (2019) 075212.

28. R.A. Youness, M.A. Taha, M. Ibrahim, A. El-Kheshen, FTIR spectral characterization, mechanical properties and antimicrobial properties of La-doped phosphate based bioactive glasses, Silicon 10 (2018): 1151-1159.

29. R.A. Youness, M.A. Taha, M. Ibrahim, Dense alumina-based carbonated fluorapatite nanobiocomposites for dental applications, Mater. Chem. Phys. 25 (2021) 123264.

30. T. Kokubo, H. Takadama, How useful is SBF in predicting in vivo bone bioactivity, Biomater. 27 (15) (2006): 2907-2915.

31. T. Kokubo, H. Kushitani, S. Sakka, T. Kitsugi, T. Yamamuro, Solutions able to reproduce in vivo surface-structure changes in bioactive glass-ceramics A-W, J. Biomed. Mater. Res. A 24 (1990): 721-734.

32. R.L. Siqueira, E.D. Zanotto, The influence of phosphorus precursors on the synthesis and bioactivity of SiO_2-CaO-P_2O_5 sol-gel glasses and glass-ceramics, J. Mater. Sci. Mater. Med. 24 (2013): 365-379.

33. S. Laasri, M. Taha, E.K. Hlil, A. Laghzizil, A. Hajjaji, Manufacturing and mechanical properties of calcium phosphate biomaterials, C.R. Mecanique 340 (2012): 715-720.

34. A. Bandyopadhyay, E.A. Withey, J. Moore, S. Bose, Influence of ZnO doping in calcium phosphate ceramics, Mater. Sci. Eng. C 27 (2007): 14-17.

35. A.A. El-Kheshen, M.F. Zawrah, M. Awad, Densification, phase composition, and properties of borosilicate glass composites containing nano-alumina and titania, J. Mater. Sci. Mater. Electron. 20 (2009): 637-643.

36. H.A. Abo-Mosallam, S.N. Salama, S.M. Salman, Formulation and characterization of glass-ceramics based on $Na_2Ca_2Si_3O_9$ $Ca_5(PO_4)_3$F-Mg_2SiO_4 system in relation to their biological activity, J. Mater. Sci. Mater. Med. 20 (12) (2009): 2385-2394.

37. D. Bellucci, A. Sola, A. Anesi, R. Salvatori, L. Chiarini, V. Cannillo, Bioactive glass/hydroxyapatite composites: mechanical properties and biological evaluation, Mater. Sci. Eng. C 51 (2015): 196-205.

38. H. Ghomi, M.H. Fathi, H. Edris, Effect of the composition of hydroxyapatite/bioactive glass nanocomposite foams on their bioactivity and mechanical properties, Mater. Res. Bull. 47 (2012): 3523-3532.

39. R. Koohkan, T. Hooshmand, M. Tahriri, D. Mohebbi-Kalhori, Synthesis, characterization and in vitro bioactivity of mesoporous copper silicate bioactive glasses, Ceram. Int. 44 (2018): 2390-2399.

40. R.L. Siqueira, N. Maurmann, D. Burguêz, D.P. Pereira, A.N.S. Rastelli, O. Peitl, P. Pranke, E.D. Zanotto, Bioactive gel-glasses with distinctly different compositions: bioactivity, viability of stem cells and antibiofilm effect against Streptococcus mutans, Mater. Sci. Eng. C 76 (2017): 233-241.

41. P.R.T. Kuzyk, E.H. Schemitsch, The science of electrical stimulation therapy for fracture healing, Indian J. Orthop. 43 (2) (2009): 127-131.

42. L. Leppik, H. Zhihua, S. Mobini, V. Thottak, K. Parameswaran, M. Eischen, A. Slavici, J. Helbing, L. Pindur, K.M.C. Oliveira, M.B. Bhavasar, L. Hudak, D. Henrich, J.H. barker, Combining electrical

stimulation and tissue engineering to treat large bone defects in a rat model, Sci. Rep. 8 (2018) 6307.

43. C. Galli, G. Pedrazzi, M. Mattioli-Belmonte, S. Guizzardi, The use of pulsed electromagnetic fields to promote bone responses to biomaterials in vitro and in vivo, Int. J. Biomater. 2018 (2018): 1-15.

44. M.M.R.A. Lima, R.C.C. Monteiro, M.P.F. Graca, M.G.F. da Silva, Structural, electrical and thermal properties of borosilicate glass-alumina composites, J. Alloys Compd. 538 (2012): 66-72.

45. K. Yamashita, K. Kitagaki, T. Umegaki, Thermal-instability and proton conductivity of ceramic hydroxyapatite at high-temperatures, J. Am Ceram Soc. 78 (1995): 1191-1197.

46. J.P. Gittings, C.R. Bowen, A.C.E. Dent, I.G. Turner, F.R. Baxter, J.B. Chaudhuri, Electrical characterization of hydroxyapatite-based bioceramics, Acta Biomater. 5 (2009): 743-754.

47. S.M. Kalil, H.H. Beheri, W.I.A. Fattah, Structural and electrical properties of zirconia/hydroxyapatite porous composites, Ceram Int. 28 (2002): 451-458.

48. K. Yamashita, H. Owada, H. Nakagawa, T. Umegaki, T. Kanazawa, Trivalent-cation-substituted calcium oxyhydoxyapatite, J. Am. Ceram. Soc. 69 (1986): 590-594.

49. T. Takahashi, S. Tanase, O. Yamamoto, Electrical-conductivity of some hydroxyapatites, Electrochim. Acta 23 (1978): 369-373.

50. E.M.A. Khalil, R.A. Youness, M.S. Amer, M.A. Taha, Mechanical properties, in vitro and in vivo bioactivity assessment of Na_2O-CaO-B_2O_3-SiO_2 glass-ceramics, Ceram. Int. 44 (2018): 7867-7876.

51. T. Kokubo, T. Hayashi, S. Sakka, T. Kitsugi, T. Yamamuro, Bonding between bioactive glasses, glass-ceramics or ceramics in a simulated body fluid, J Ceram Soc. Jpn. 95 (8) (1987): 785-791.

52. S.H. Oh, S.Y. Choi, Y.K. Lee, K.N. Kim, Research on annihilation of cancer cells by glass-ceramics for cancer treatment with external magnetic field. I. Preparation and cytotoxicity, J. Biomed. Mater Res 54 (3) (2001): 360-36524.

53. T. Kokubo, S. Ito, S. Sakka, T. Yamamuro, Formation of a high-strength bioactive glass-ceramic in the system MgO-CaO-SiO_2-P_2O_5, J Mater Sci 21 (2) (1986): 536-540.

54. H.A. El Batal, M.A. Azooz, M.M. Ibrahim, A.M. Ali, H.H. Somaily, M.A. Sayed, Bioactivity behavior of multicomponent (P_2O_5-B_2O_3-SiO_2-Na_2O-CaF_2) glasses doped with ZnO, CuO or Ag_2O and their glass ceramics, Silicon (2020) In Press.

55. L. Radev, I. Michailova, D. Zaimova, T. Dimova, In vitro bioactivity of silver containing sol-gel glasses: FTIR analysis, IJIR 3 (4) (2017): 316-323.

56. M. Htut, M. Lwin, P. Kaung, S. Htoon, Infrared spectroscopic study on the structure of $Ag_2O.B_2O_3$ glasses, Jour. Myan. Acad. Arts& Sc. IV (2) (2000): 339-346.

57. J.A. Roether, A.R. Boccaccini, L.L. Hench, V. Maquet, S. Gautier, R. Jerome, Development and in vitro characterization of novel bioresorbable and bioactive composite materials based on polylactide foams and bioglass for tissue engineering applications, Biomaterials 23 (2002): 3871-3878.

58. W.S. AbuShanab, E.B. Moustafa, M.A. Taha, R.A. Youness, Synthesis and structural properties characterization of titania/zirconia/calcium silicate nanocomposites for biomedical applications,

Appl. Phys. A 126 (2020): 1-12.

59. O.G. Agbabiaka, I.O. Oladele, A.D. Akinwekomi, A.A. Adediran, A.O. Balogun, O.G. Olasunkanm, T.M.A. Olayanju, Effect of calcination temperature on hydroxyapatite developed from waste poultry eggshell, Sci. African 8 (2020) e00452.

60. W.P.S.L. Wijesinghe, M.M.M.G.P.G. Mantilaka, E.V.A. Premalal, H.M.T.U. Herath, S. Mahalingam, M. Edirisinghe, R.P.V.J. Rajapakse, R.M.G. Rajapakse, Facile synthesis of both needle-like and spherical hydroxyapatite nanoparticles: effect of synthetic temperature and calcination on morphology, crystallite size and crystallinity, Mater. Sci. Eng. C 42 (2014): 83-90.

61. X. Guo, H. Yan, S. Zhao, L. Zhang, Y. Li, X. Liang, Effect of calcining temperature on particle size of hydroxyapatite synthesized by solid-state reaction at room temperature, Adv. Powder Technol. 24 (2013): 1034-1038.

Figures
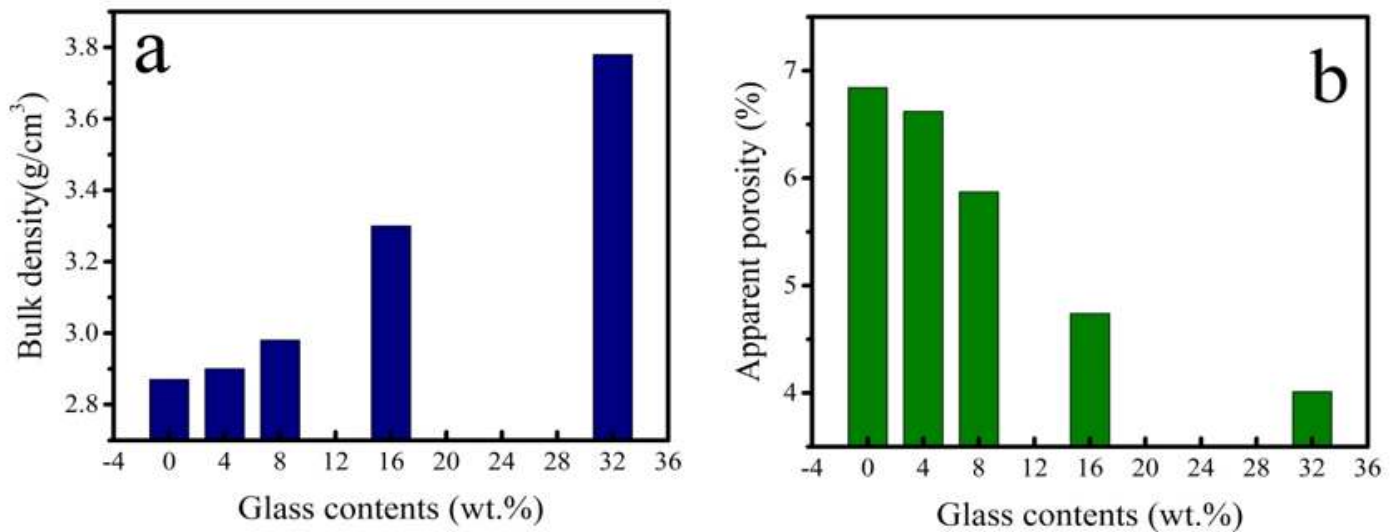
Figure 1

a) Bulk density and b) apparent porosity of the prepared nanocomposites versus BG content. This figure shows that the sinterability of the tested samples is enhanced by increasing the BG content.
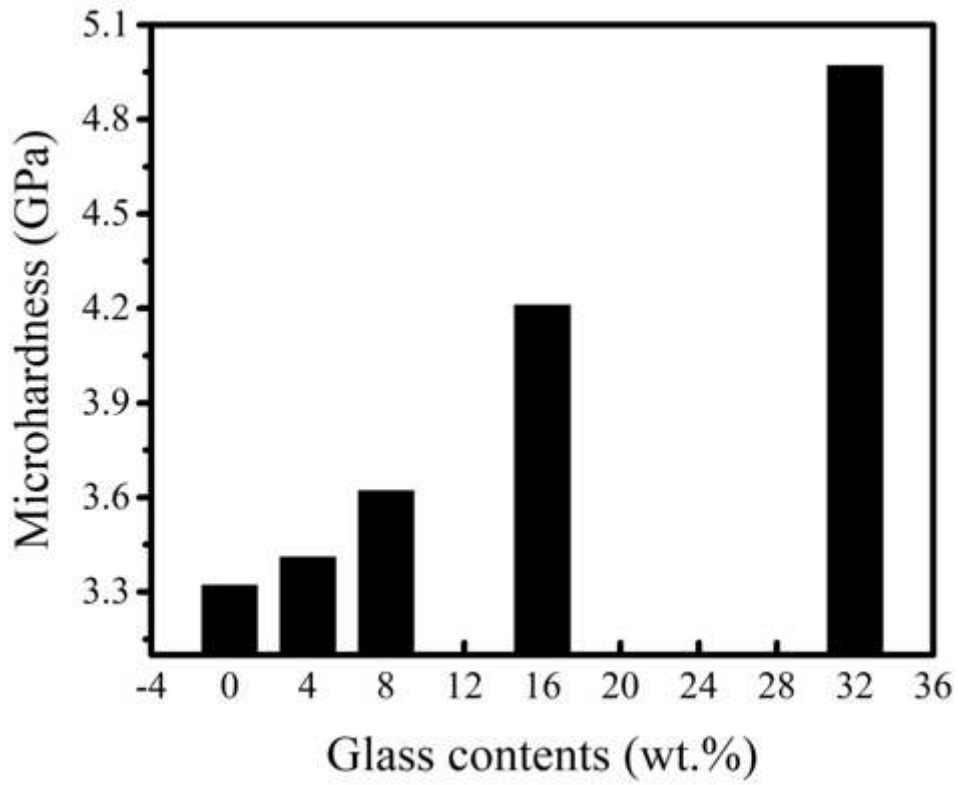
Figure 2

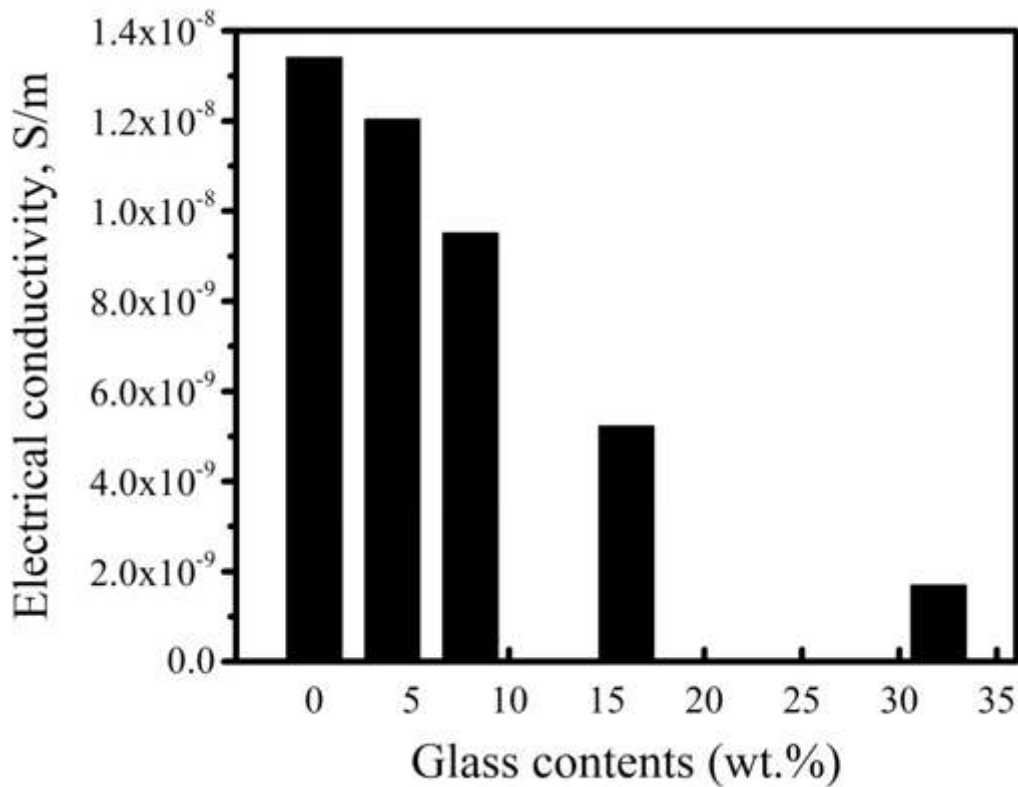Microhardness of the prepared CHA/BG nanocomposites sintered at 750 °C.
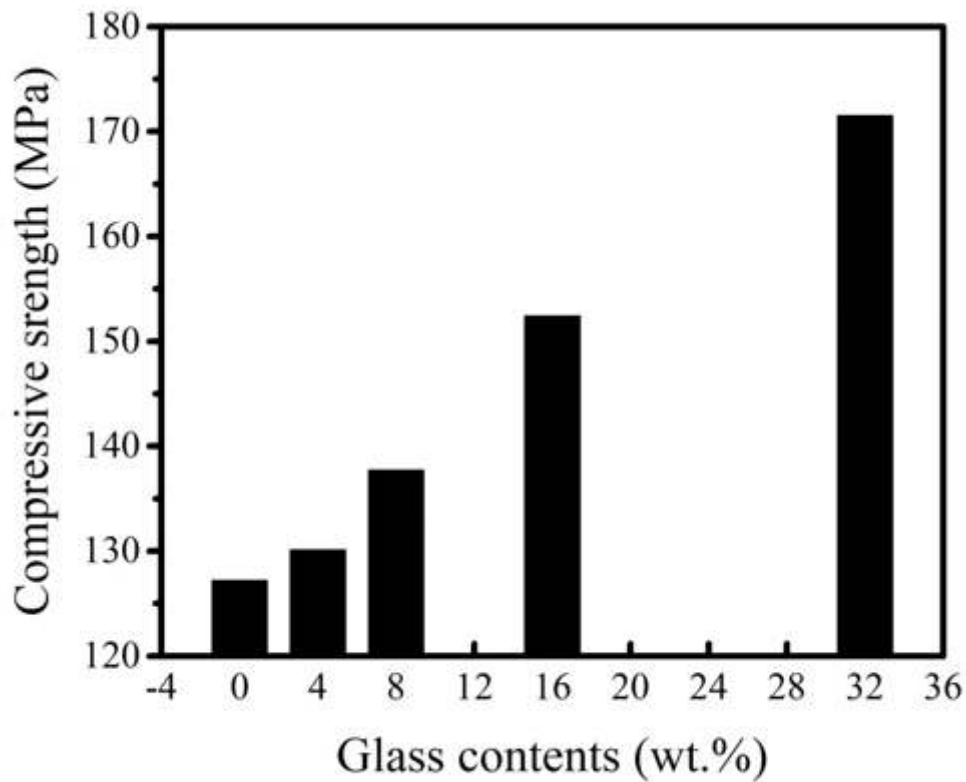
Figure 3

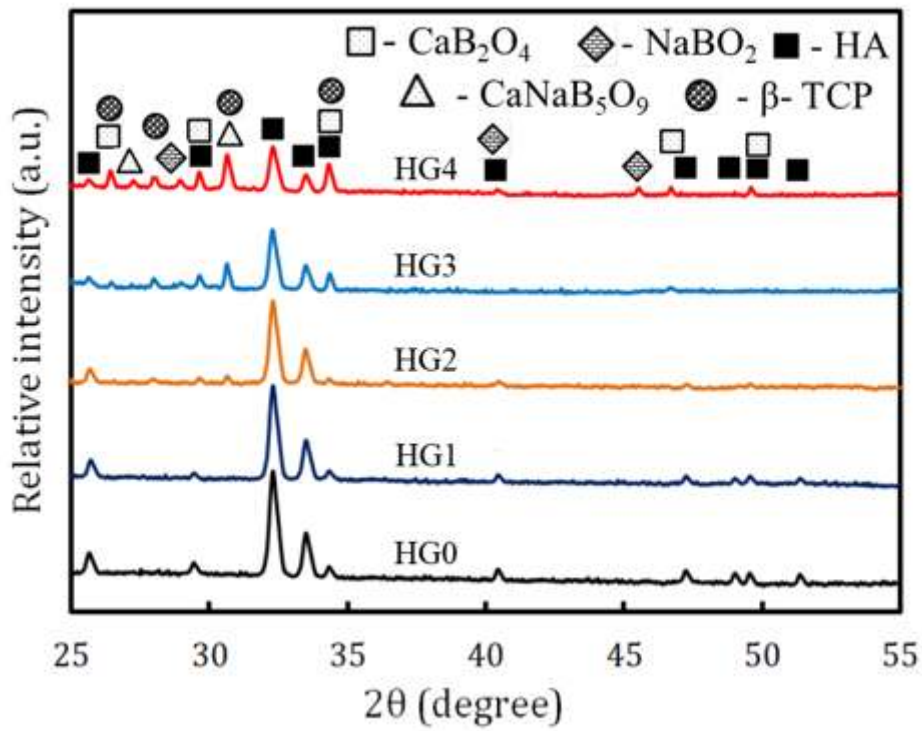The compressive strength of the prepared CHA/BG nanocomposites sintered at 750 °C.
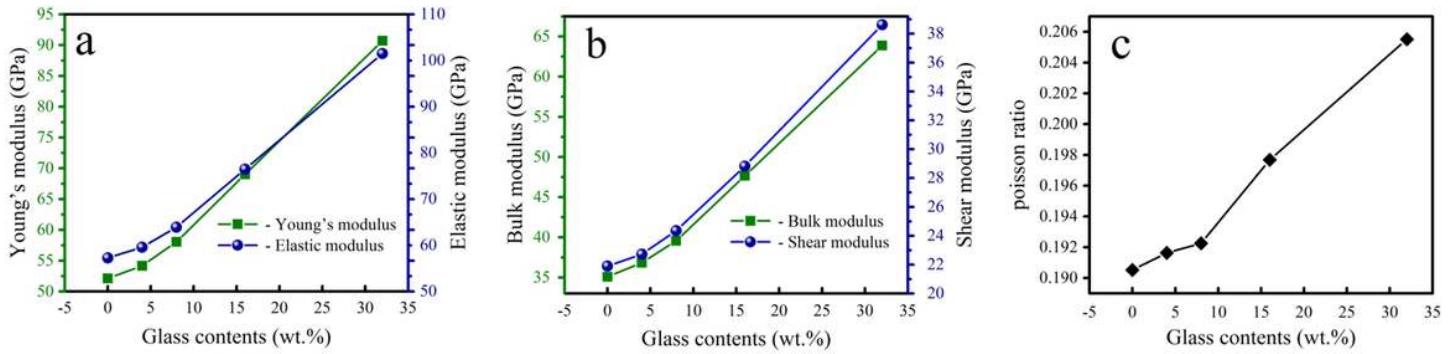
Figure 4

The different mechanical properties of the sintered nanocomposites in terms of a) Young's and elastic moduli, b) bulk and shear moduli and c) Poisson's ratio.

Figure 5

DC electrical conductivity values for CHA/BG nanocomposites.

Figure 6

XRD patterns of sintered nanocomposites indicating the gradual formation of CaB2O4, Na2BO2, CaNaB5O9, Ag2O and Ca3(PO4)2 phases due to successive increases in BG content beside Ca10(PO4)6(OH)2
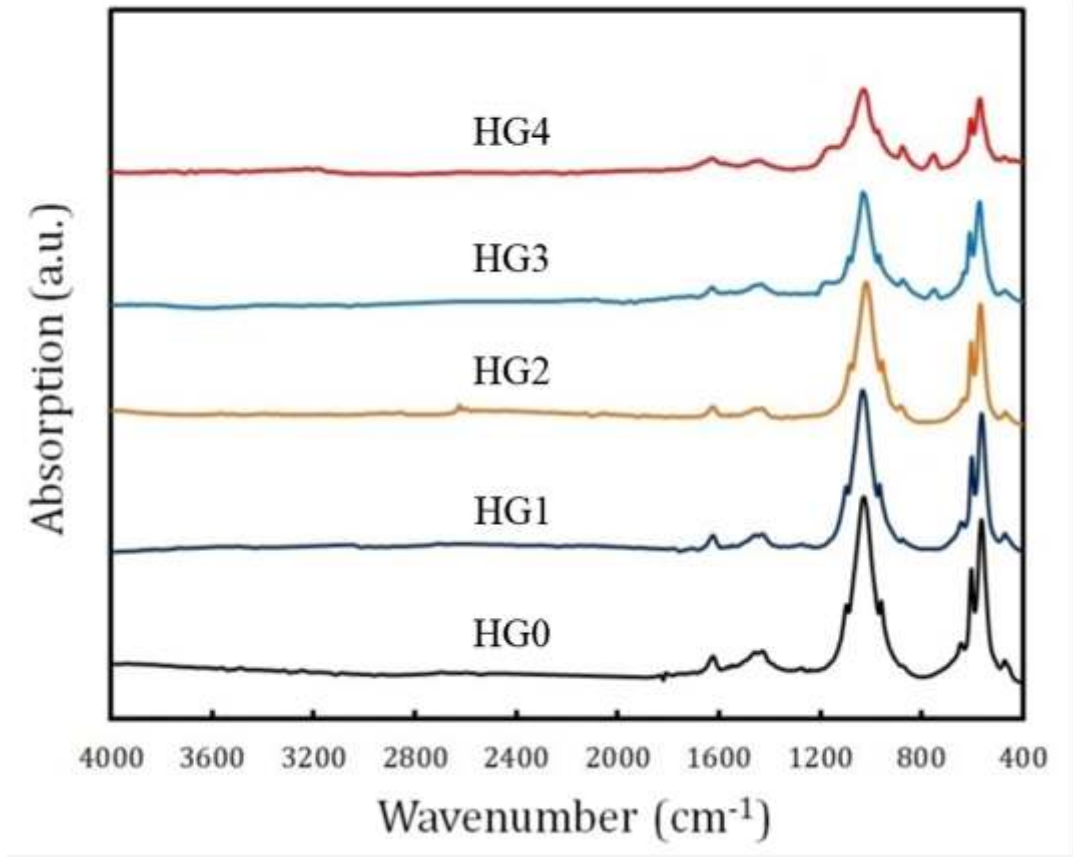
Figure 7

FTIR absorption spectra of sintered nanocomposites showing a gradual decrease in the intensity of the bands at 1635, 1470, 1420, 1100, 1035, 960, 870, 603, 633 and 560 cm-1 with increasing BG content.
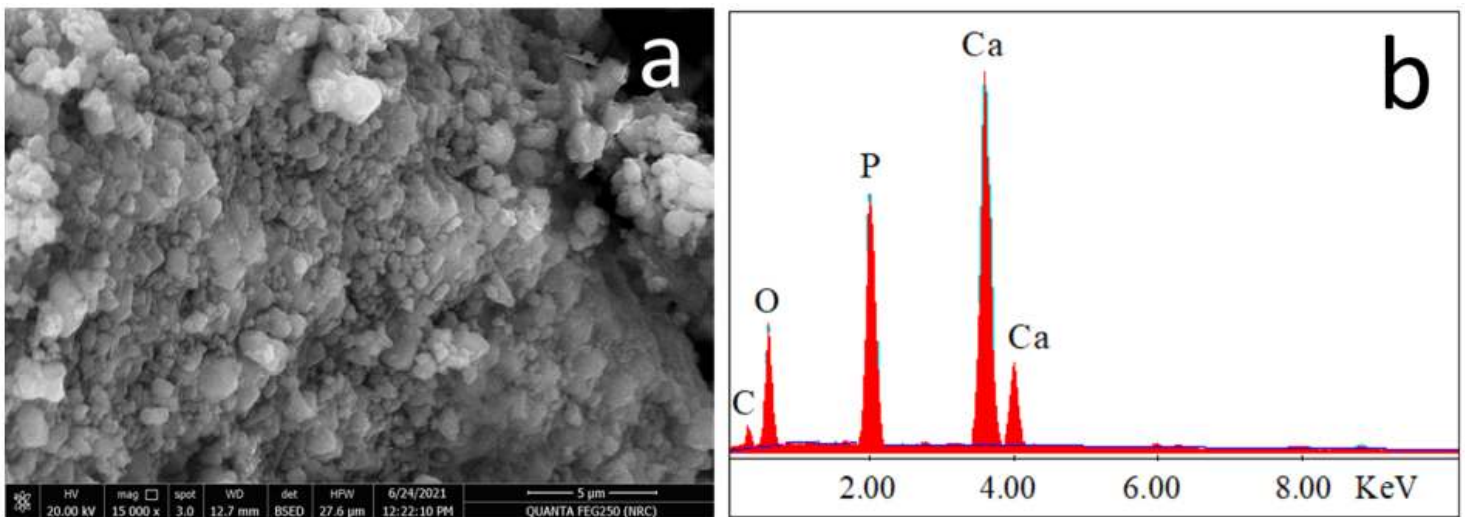

Figure 8

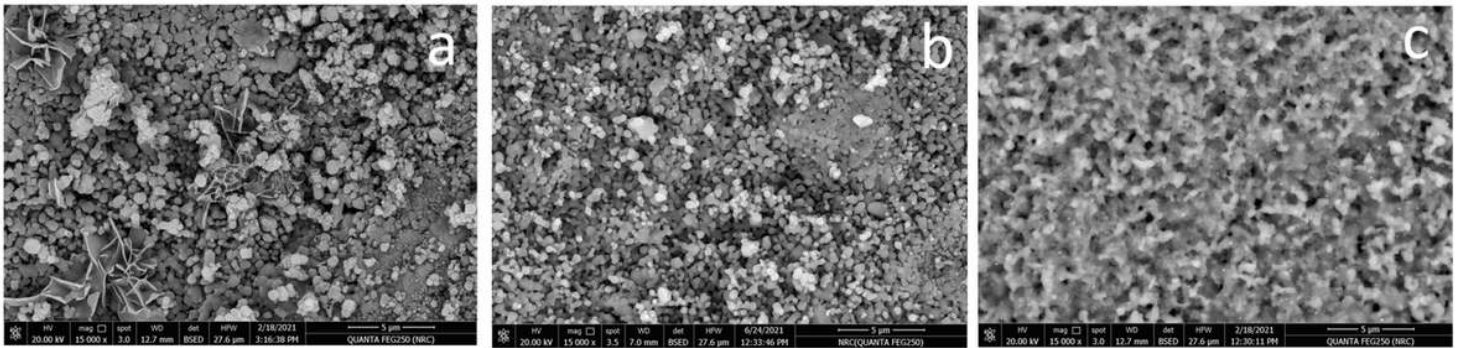a) SEM micrograph and b) EDS spectrum of the as-prepared CHA nanopowders.

Figure 9

SEM images of sintered a) HG0, b) HG2 and c) HG4 samples.
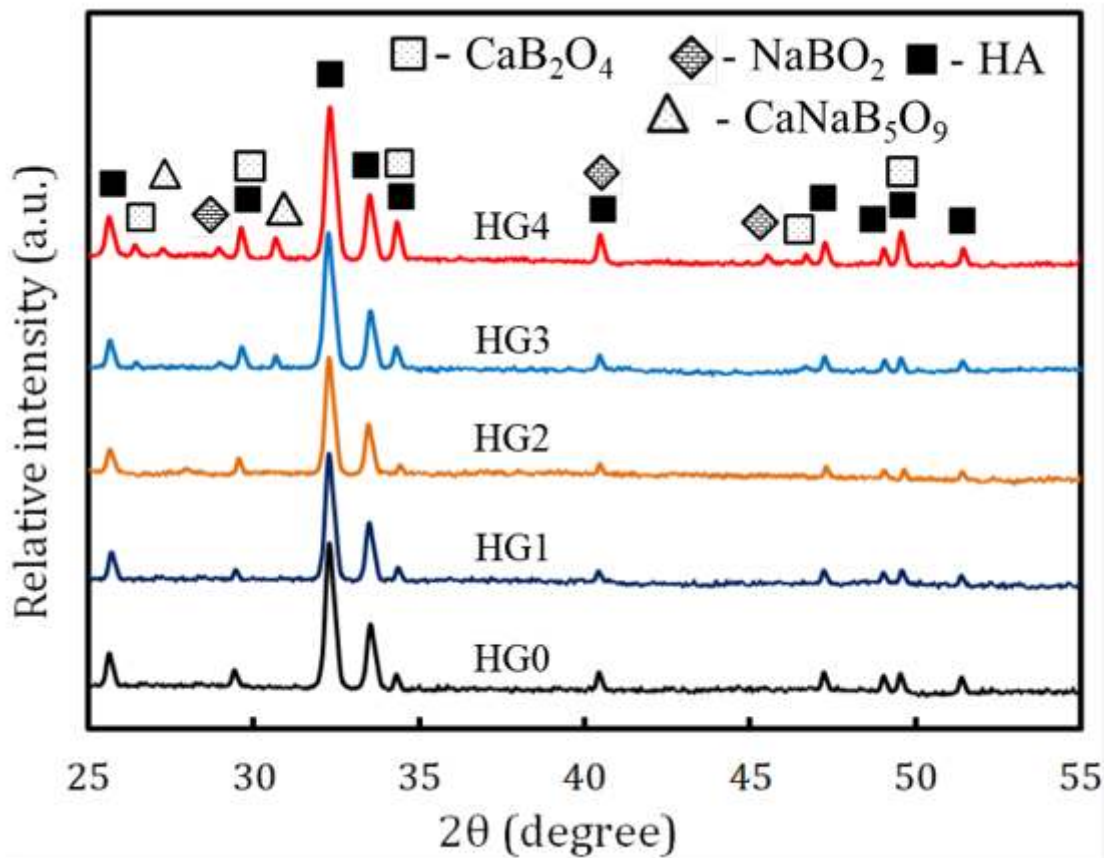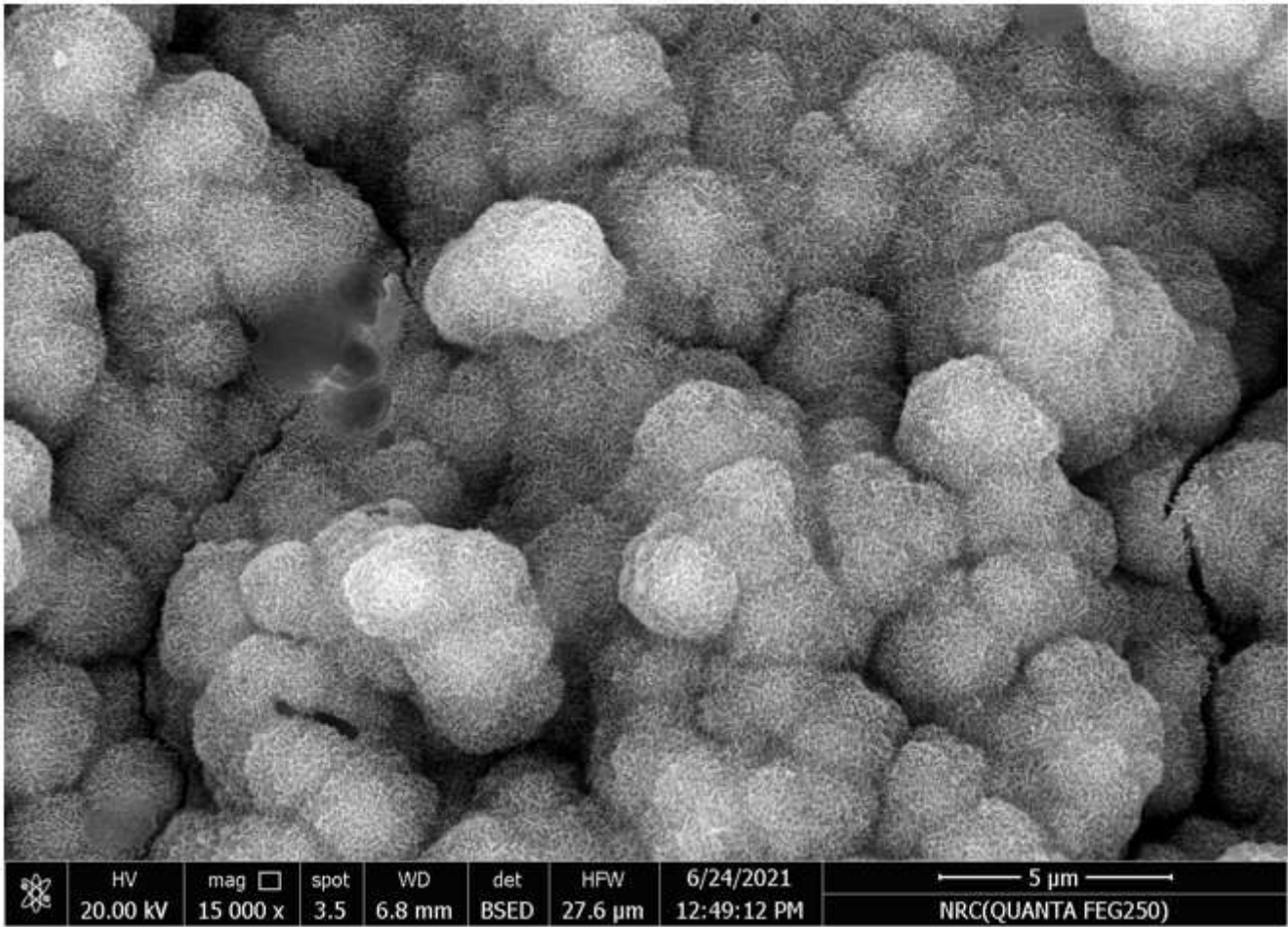

Figure 10

XRD patterns of sintered nanocomposites after soaking in SBF solution for 10 days. This figure reveals that the best bioactivity behavior is for the HG4 sample.

Figure 11

SEM image of a sintered HG4 sample after soaking in SBF solution for 10 days.